Magnetic and ferroelectric orderings in multiferroic α-$NaFeO_2$

Noriki Terada,[1,2,4,*] Dmitry D. Khalyavin,[2] Juan M. Perez-Mato,[3] Pascal Manuel,[2] Dharmalingam Prabhakaran,[4] Aziz Daoud-Aladine,[2] Paolo G. Radaelli,[4] Hiroyuki S. Suzuki,[1] and Hideaki Kitazawa[1]

[1]*National Institute for Materials Science, Sengen 1-2-1, Tsukuba, Ibaraki 305-0047, Japan*

[2]*ISIS Facility, STFC Rutherford Appleton Laboratory, Chilton, Didcot, Oxfordshire, OX11 0QX, United Kingdom*

[3]*Departamento de Fisica de la Materia Condensada, Facultad de Ciencia y Tecnologia, Universidad del Pais Vasco, UPV/EHU, Apartado 644, E-48080 Bilbao, Spain*

[4]*Clarendon Laboratory, Department of Physics, University of Oxford, Parks Road, Oxford OX1 3PU, United Kingdom*

(Received 14 April 2014; published 28 May 2014)

The triangular based antiferromagnet α-$NaFeO_2$ has been studied by magnetization, dielectric, and neutron diffraction measurements as a function of temperature and magnetic field. The appropriate $(H-T)$ phase diagram was constructed revealing a complex behavior due to a competition between several magnetic phases. In zero field, the system undergoes a sequence of magnetostructural transitions; initially from paramagnetic $R\bar{3}m1'$ phase to the incommensurate spin density wave (ICM1) at $T_{N1} = 11$ K with the nonpolar (3+1) magnetic superspace group $C2/m1'(0,\beta,\frac{1}{2})s0s$, then, below $T_{N2} = 7.5$ K, the ICM1 phase coexists with the polar cycloidal ordering (ICM2) possessing the $Cm1'(0,\beta,\frac{1}{2})0s$ superspace symmetry and finally the commensurate collinear ordering (CM) with the nonpolar magnetic space group P_a2_1/m develops below $T_{N3} = 5.5$ K as the ground state of the system. A small amount of ICM2 coexists with the ICM1 and CM phases resulting in a nonzero measured polarization below T_{N2}. Magnetic field destabilizes the collinear ground state and promotes the polar ICM2 phase resulting in a drastic increase of the polarization. The symmetry of the zero field cycloidal structure allows the two orthogonal components $\boldsymbol{p}_1 \propto \boldsymbol{r}_{ij}\times(\boldsymbol{S}_i\times\boldsymbol{S}_j)$ and $\boldsymbol{p}_2 \propto \boldsymbol{S}_i\times\boldsymbol{S}_j$ to contribute to the macroscopic polarization through the inverse DM effect. The applied magnetic field reduces the symmetry of the ICM2 phase down to the triclinic $P1(\alpha,\beta,\gamma)0$, resulting in admixture of another cycloidal and helical components both generating magnetic field switchable polarization $\boldsymbol{p}_3$ perpendicular to $\boldsymbol{p}_1$ and $\boldsymbol{p}_2$.

DOI: 10.1103/PhysRevB.89.184421 PACS number(s): 75.80.+q, 75.50.Ee, 77.80.−e

I. INTRODUCTION

Multiferroic materials with ferroelectricity and noncollinear magnetic ordering have attracted much attention in the last decade [1–3]. Some spiral spin arrangements, which occur as a consequence of spin frustration, break inversion symmetry and induce a ferroelectric polarization through inverse Dzyaloshinsky-Moriya (DM) effect. The mechanisms responsible for the ferroelectric polarization in rare earth manganites $ReMnO_3$ (Re = Tb, Dy, Gd, etc.) have been discussed in several theoretical studies [4–6], which introduced the expression $\boldsymbol{p} \propto \boldsymbol{r}_{ij}\times(\boldsymbol{S}_i\times\boldsymbol{S}_j)$ to explain the direction of P. However, this formula does not work for multiferroics with proper screw type helical ordering such as $RbFe(MoO_4)_2$ [7,8], $Cu_3Nb_2O_8$ [9], $CaMn_7O_{12}$ [10], $CuFeO_2$ [11–15], and $CuCrO_2$ [16,17]. In the first three compounds, the authors explained the ferroelectricity by a coupling between the spin chirality $\boldsymbol{r}_{ij}\cdot(\boldsymbol{S}_i\times\boldsymbol{S}_j)$ and ferroaxial crystal rotation $\boldsymbol{A}$ based on inverse DM effect [8–10]. On the other hand, the ferroelectric polarizations in the latter two multiferroics have been attributed to the spin-dependent $d-p$ hybridization [18] and later to the inverse DM effect as well [19].

ABO_2 type compounds are typical and nearly ideal examples of frustrated triangular lattice antiferromagnets [20]. In 2006, Kimura *et al.* discovered the ferroelectric polarization induced by a magnetic field in $CuFeO_2$, which is concomitant with a collinear to noncollinear magnetic phase transition at $H = 7$ T [11]. Since that time, several other ABO_2 materials, such as $CuCrO_2$ [16,17,21], $CuFe_{1-x}B_xO_2$ (B = Al and Ga) [12–15], and $AgFeO_2$ [22], have been investigated to understand the interrelation between noncollinear spin ordering and the ferroelectric polarization. Various magnetic structures in these compounds occur in zero magnetic field; a collinear in $CuFeO_2$ [23,24], proper screw helix in $CuCrO_2$ [25], and a cycloid in $AgFeO_2$ [22]. Thus, ABO_2 type triangular lattice antiferromagnets provide great opportunities to study the interplay between frustrated magnetism and ferroelectric properties.

In the present work we selected one of the ABO_2 type of materials, namely α-$NaFeO_2$, in order to study its magnetic and dielectric properties under influence of a high magnetic field. α-$NaFeO_2$ has the ordered rock-salt crystal structure with the space group $R\bar{3}m$ similar to the delafossites compounds (Fig. 1). The only difference between the two structures is in the oxygen coordination of the A sites (straight bond along the hexagonal c axis in delafossites and octahedral coordination in the ordered rock-salt structure). The magnetic properties of α-$NaFeO_2$ have been reported in several previous studies [26–28]. In particular, two magnetic phase transitions were found to occur at 10.5 and 5 K in zero magnetic field. In the temperature range $5 \leqslant T \leqslant 10.5$ K, incommensurate magnetic ordering with temperature dependent propagation vector $\boldsymbol{k} = (q,q,\frac{3}{2},q \simeq 0.12)$ was observed [28]. Below 5 K, the commensurate magnetic state with collinear moments along the hexagonal b axis and $\boldsymbol{k} = (\frac{1}{4},0,1)$ has been identified as the magnetic ground state [26,28]. In a recent study by McQueen *et al.* [28], a pronounce changes of the magnetic susceptibility have been revealed in magnetic fields below 5 T,

*TERADA.Noriki@nims.go.jp

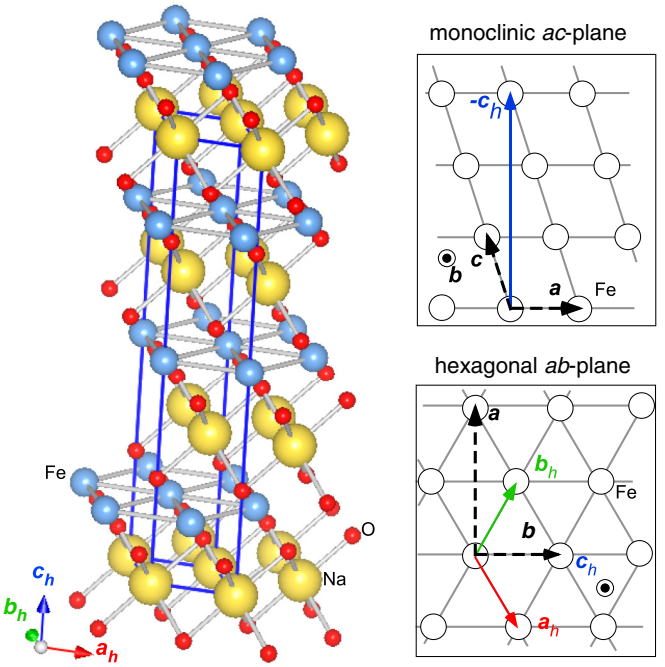

FIG. 1. (Color online) (Left) Ordered rock-salt type crystal structure of α-$NaFeO_2$. (Right) Relationship between the hexagonal and monoclinic basis vectors [$\boldsymbol{a} = \boldsymbol{b}_h - \boldsymbol{a}_h$, $\boldsymbol{b} = \boldsymbol{a}_h + \boldsymbol{b}_h$, $\boldsymbol{c} = \frac{1}{3}(\boldsymbol{a}_h - \boldsymbol{b}_h - \boldsymbol{c}_h)$, Fe is at the origin].

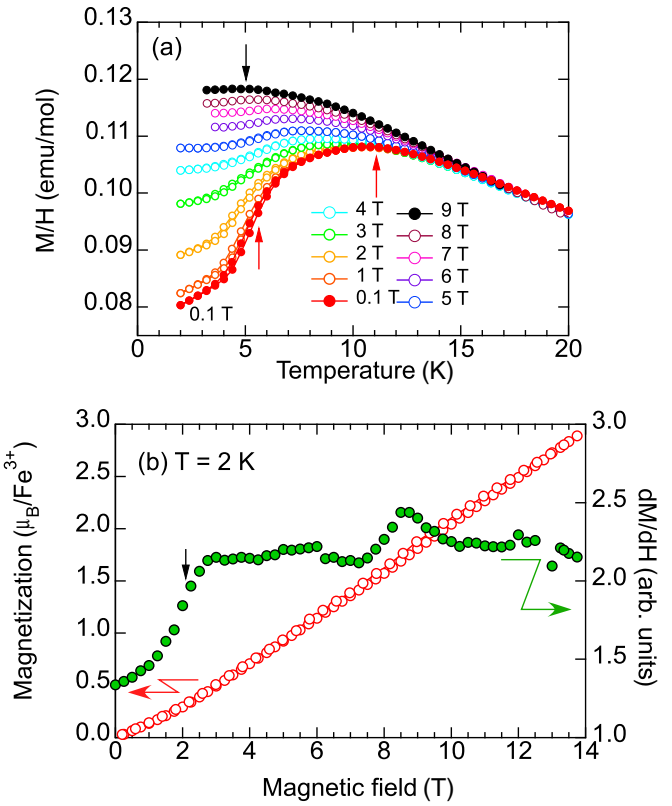

FIG. 2. (Color online) (a) Temperature dependencies of magnetization for α-$NaFeO_2$, measured in different magnetic fields. The data were normalized to the field and scaled to match the value at $T = 20$ K and $H = 0.1$ T. (b) The magnetization (open circles) and its derivative with respect to the magnetic field (closed circles) at $T = 2$ K. Vertical arrows indicate the temperatures and field where anomalies appear.

indicating a rich $H - T$ phase diagram for α-$NaFeO_2$. To elucidate details of this diagram, we undertook magnetization, dielectric constant, pyroelectric current, and neutron diffraction measurements as a function of temperature and magnetic field.

II. EXPERIMENTAL DETAILS

Powder samples of α-$NaFeO_2$ were prepared by solid state reaction method using Na_2CO_3 and γ-Fe_2O_3 as the starting materials [29]. The latter was obtained by annealing of Fe_3O_4 at 300 °C for 2 h in oxygen gas flow. The reaction was performed during 24 h in air. X-ray powder diffraction measurements confirmed the phase formation and a good quality of the sample. Small amounts of impurity phases β-$NaFeO_2$ (∼3.5%) and Na_2CO_3 (∼0.5%) were detected, however, in the neutron diffraction experiments and included in the refinement procedures.

For the low-field ($H \leqslant 5$ T) and high-field ($H \leqslant 13.5$ T) magnetization measurements, we used a magnetic-property measurement system (MPMS) and a physical property measurement system (PPMS), respectively, both manufactured by Quantum Design. The dielectric constant and pyroelectric current measurements were done by Agilent E4980A LCR meter and Keithley 6517B electrometer combined with PPMS. The dielectric properties were measured using 0.80 mm of thickness and hardened pellets of the polycrystalline α-$NaFeO_2$ sample, covered with 13.8 mm^2 area of silver paste.

The neutron powder diffraction measurements were carried out on the time-of-flight diffractometers HRPD [30] for the crystal structure determination in zero magnetic field and WISH [31] for the magnetic structure analysis under magnetic fields up to 10 T, both situated at the ISIS Facility of the Rutherford Appleton Laboratory (UK). For the HRPD measurement, we used approximately a 3 g powder sample of α-$NaFeO_2$ sealed into a plate shape vanadium can with He gas atmosphere. For the experiments under magnetic fields on WISH, we prepared rods of 6 mm diameter and 20 mm long, pressed from the powder to avoid any realignment of the grains under magnetic fields. In fact, there was no difference, within the experimental accuracy, in the diffraction data collected before and after applying the magnetic field. To investigate the sample dependent features in the magnetic diffraction data, we measured two different samples (sample1 and sample2) on the WISH diffractometer, which were synthesized separately. The vertical magnetic field was generated in the cryomagnet manufactured by Oxford Instruments [32], which has a 340 deg in-plane window matching the detector array and a wide vertical opening angle (−5, +10 deg). The crystal and magnetic structure refinements were performed using the FullProf program [33].

III. RESULTS

A. Bulk properties

Temperature dependencies of the magnetization for α-$NaFeO_2$ measured in several magnetic fields are shown in

Fig. 2(a). In $H = 0.1$ T, the magnetization shows a maximum at 10.5 K and a steep change at 5.5 K as indicated by the arrows. With increasing the magnetic field up to 9 T, both anomalies shift to lower temperature, which is consistent with the previous results [28]. The maximum of the magnetization in 9 T is observed at 5 K, and the lower phase transition is invisible in this field. The magnetization of α-$NaFeO_2$ as a function of the field at $T = 2$ K is shown in Fig. 2(b). The value of the derivative is steeply changed by the applied magnetic field around $H_c \simeq 2.5$ T, indicating a spin-flop-like phase transition. We also found a broad peak at ~8.5 T, suggesting another possible change in the magnetic state, as will be discussed later.

As demonstrated in Fig. 3(a), the ferroelectric polarization was observed in all measured magnetic fields, although the absolute values of P depend on the magnetic field significantly. In zero field, P appears below 7.5 K and shows a shoulderlike anomaly at 5.5 K, which is consistent with the two broad peaks in the imaginary part of the dielectric constant ϵ_r'' shown in Fig. 3(c). With increasing magnetic field, P is significantly enhanced around 2–3 T, where the spin-flop-like transition occurs [see also Fig. 9(c)]. Above 7 T, P weakly depends on the field and stays close to the value of 60 μC/m^2. In respect of the electric field effect E_p, the polarization is not saturated even at $E_p = 500$ kV/m as shown in the inset of Fig. 3(a). The peak anomalies in the dielectric constants, which are presented in Figs. 3(b) and 3(c), are also enhanced by the magnetic fields, especially ϵ_r'', suggesting the ferroelectric phase transition becomes clear in the high magnetic field region.

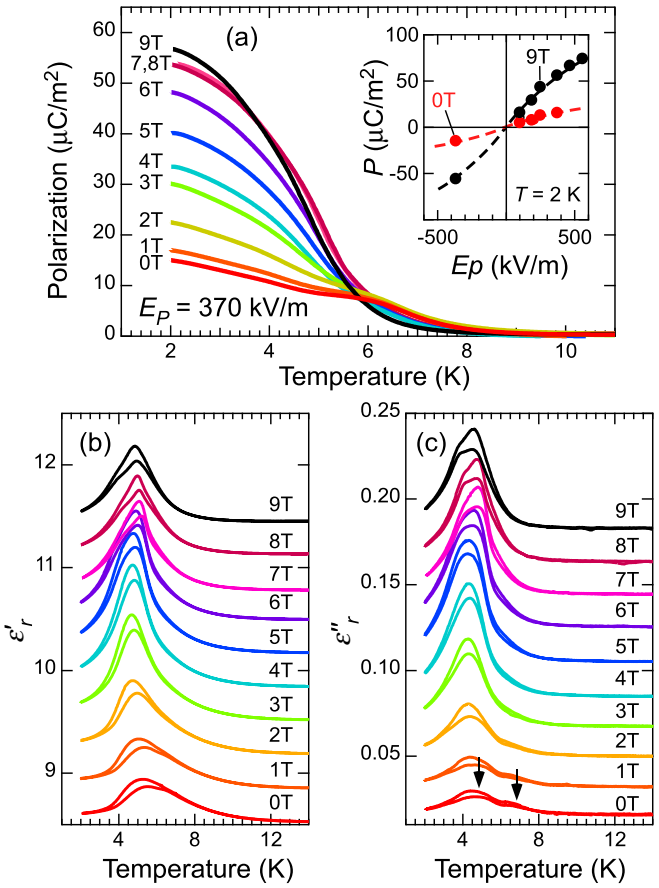

FIG. 3. (Color online) Temperature dependence of (a) electric polarization, (b) real, and (c) imaginary parts of the relative dielectric constants in magnetic fields up to 9 T for α-$NaFeO_2$. Polarization as a function of the poling electric field E_p at $H = 0$ and 9 T are shown in the inset of (a).

B. NEUTRON DIFFRACTION

1. Magnetic orderings in zero magnetic field

Based on the HRPD and WISH backscattering data revealing a clear splitting of some nuclear peaks below $T_{N1} = 11$ K (not shown), a symmetry lowering from the rhombohedral $R\bar{3}m$ down to monoclinic $C2/m$ can be concluded. Details of the crystal structure analysis are not discussed here and will be reported elsewhere. In addition, a set of magnetic Bragg reflections appears below this temperature (Fig. 4). In the temperature range $8 \leqslant T \leqslant 11$ K (ICM1 phase), these reflections, indicated by arrows with solid line, can be indexed with the incommensurate propagation vector $\boldsymbol{k} = (0, q_b, \frac{1}{2})$ ($\equiv \boldsymbol{k}_{\mathrm{ICM1}}$), with $q_b \simeq 0.238$ referring to the monoclinic setting shown in Fig. 1 (right). Hereafter the propagation vectors and indexation are given by default for the monoclinic setting. The wave number q_b is practically independent of temperature in the whole region of stability of the ICM1 phase [Fig. 6(b)]. The reciprocal plane illustrating the relation between the hexagonal and the monoclinic indexing schemes is shown in Fig. 5(a). The $\boldsymbol{k}_{\mathrm{ICM1}}$ corresponds to the $(q,q,3/2)$ propagation vector with

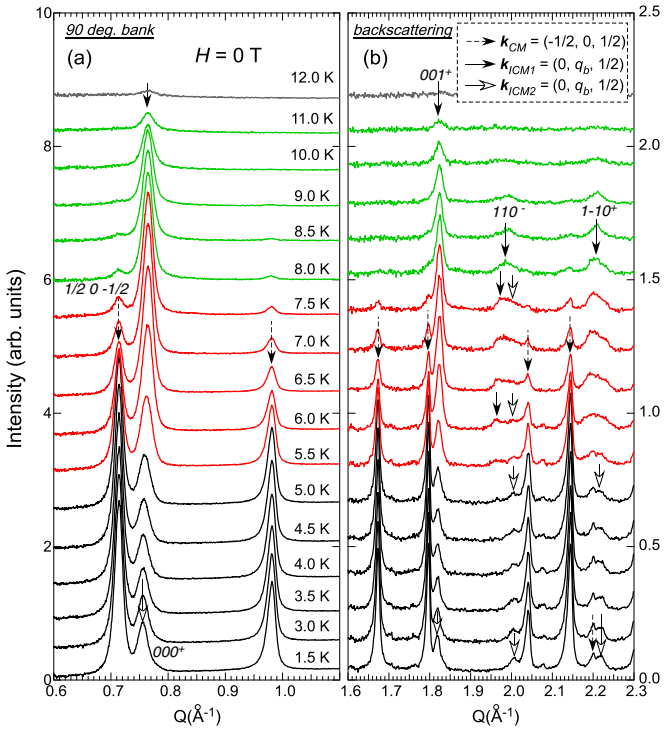

FIG. 4. (Color online) Temperature dependence of the neutron powder diffraction profiles measured in zero magnetic field for α-$NaFeO_2$. The patterns were collected using (a) 90 deg and (b) backscattering detector banks on WISH. The data at 16 K in the paramagnetic phase were subtracted from the low temperature patterns. All data were taken on heating after cooling down to the base temperature 1.5 K.

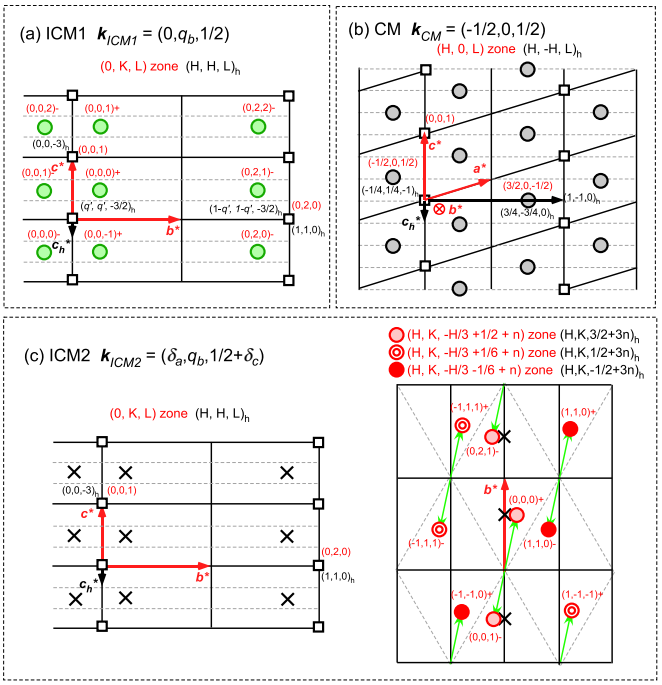

FIG. 5. (Color online) Schematic drawings of the reciprocal lattice zone for (a) ICM1, (b) CM, and (c) ICM2 phases. Circle and square symbols are the positions of the magnetic and nuclear reflections, respectively. Crosses in (c) indicate the projected positions of the magnetic reflection of ICM2 phase to the monoclinic $(0,K,L)$ zone. Solid and dotted lines denote the monoclinic and hexagonal reciprocal lattice unit cells, respectively. The subscripts (m/h) and superscripts $(+/-)$ indicate monoclinic/hexagonal and $+\boldsymbol{k}/-\boldsymbol{k}$ satellites, respectively

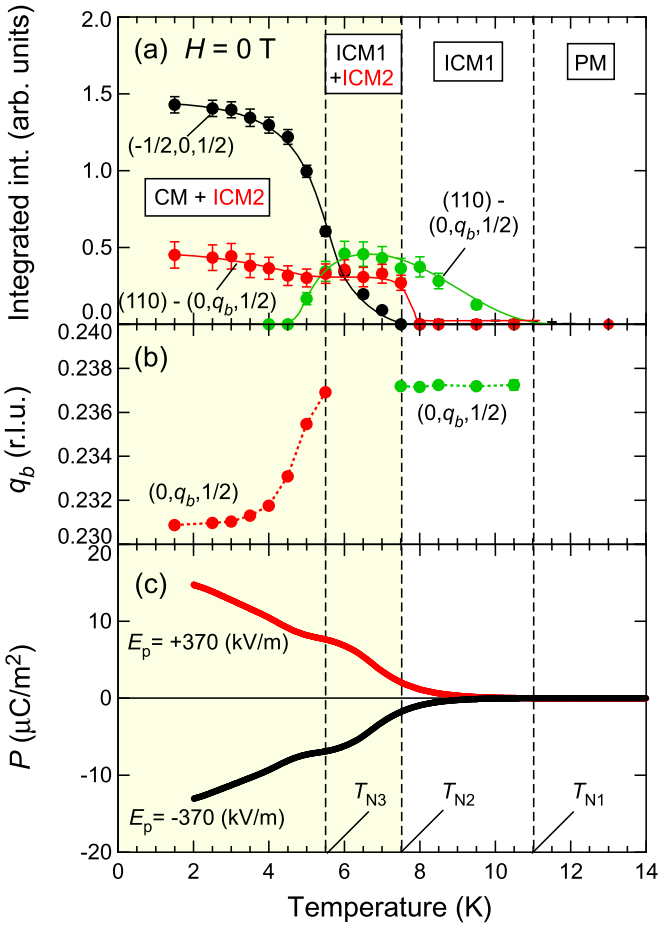

FIG. 6. (Color online) Temperature dependencies of (a) the integrated intensity of the incommensurate 110^- and the commensurate $-\frac{1}{2},0,\frac{1}{2}$ reflections, (b) the incommensurate wave number q_b, and (c) the ferroelectric polarization. Vertical dotted lines indicate the phase transition temperatures.

$q = q_b/2 \simeq 0.12$, in the hexagonal setting, which is consistent with the previous study by McQueen *et al.* [28].

As shown by the open arrows in Fig. 4(b), additional peaks can be observed below $T_{N2} = 7.5$ K, which coincide with the appearance of the polarization in zero field and indicate development of a magnetic phase (ICM2). These additional peaks, surviving even at the lowest temperature measured, can be indexed by the $\boldsymbol{k} = (0,q_b,\frac{1}{2})$ ($\equiv \boldsymbol{k}_{\rm ICM2}$) propagation vector with $q_b \simeq 0.231$ at 1.5 K. Because the magnetic peaks for the ICM2 phase coexist with those for the ICM1 phase and the propagation vectors in both phases are almost the same, we could not resolve enough number of magnetic peaks to reliably determine the spin ordering in the intermediate temperature range $5.5 \leqslant T \leqslant 7.5$ K.

At $T_{N3} = 5.5$ K, the magnetic Bragg intensity of the ICM1 phase vanishes, and a set of new reflections indexed by the commensurate (CM) $\boldsymbol{k} = (-\frac{1}{2},0,\frac{1}{2})$ ($\equiv \boldsymbol{k}_{\rm CM}$) propagation vector appears as shown in Fig. 6(a). The CM magnetic Bragg points in the reciprocal lattice are illustrated in Fig. 5(b), indicating that $\boldsymbol{k}_{\rm CM}$ in the hexagonal setting is $(-\frac{1}{4},\frac{1}{4},-1)$. The magnetic intensity of the ICM2 phase remains even at the lowest measured temperature, and the volume fractions for CM and ICM2 slightly depend on samples. Nevertheless, the dominant phase at the base temperature 1.5 K is always the CM one. Thus, one can conclude that the CM spin ordering represents the magnetic ground state of α-$NaFeO_2$ in zero field, but this phase always coexists with a minor fraction of ICM2 state indicating that both phases are almost degenerate.

For the ICM1 phase with $\boldsymbol{k}_{\rm ICM1} = (0,q_b,\frac{1}{2})$ we found that the magnetic order parameter transforms as the time-odd mY_1 irreducible representation (in the ISODISTORT notations [34]) of the $R\bar{3}m1'$ space group, reducing the symmetry down to the (3+1) monoclinic superspace group $C2/m1'(0,\beta,\frac{1}{2})s0s$ ($\beta = q_b$) [34,35]. Thus, the $C2/m$ symmetry found in the high resolution neutron diffraction experiments, is the commensurate approximation for the nuclear structure, corresponding to zeroth harmonic of the magnetic superspace group, which takes into account only coupling to the macroscopic symmetry-breaking strain components. Detection of the higher order harmonics is beyond sensitivity of our diffraction experiments. The refinements of the neutron diffraction patterns were done using the propagation vectors formalism implemented into the FullProf package. The nuclear scattering was modeled in the commensurate $C2/m$ approximation and the magnetic structure was successfully refined assuming collinear SDW with the magnetic moments being in the (ac) plane as restricted by the mY_1 representation. The quality of the fitting for the data measured at 9 K and a schematic

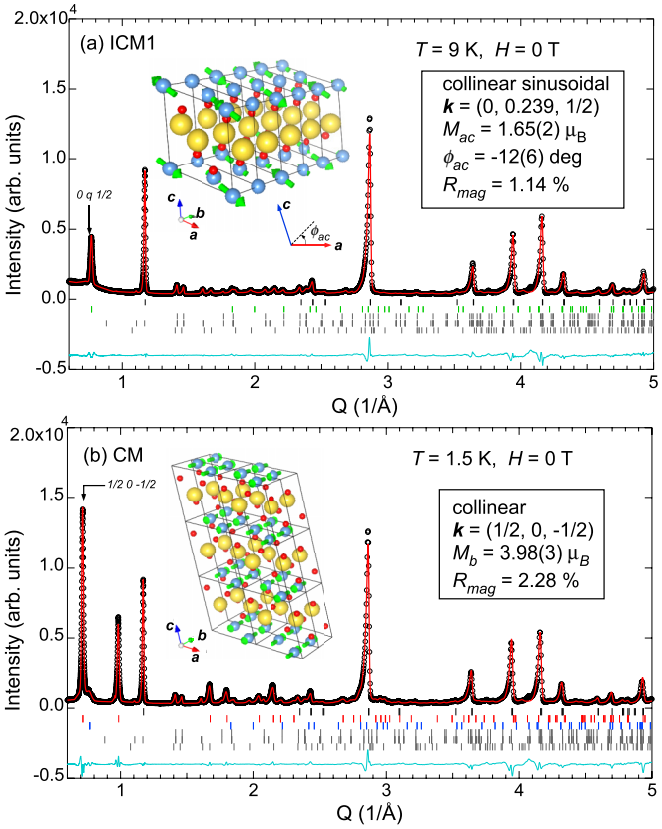

FIG. 7. (Color online) Refinement quality of the WISH data measured at (a) 9 K and 0 T and (b) 1.5 K and 0 T. The first line of the vertical bars indicate the peak positions for the crystallographic main phase of α-$NaFeO_2$. The second line in (a), and the second and the third lines in (b) are for the spin-density wave, the collinear commensurate, and a cycloid magnetic structures, respectively. The other three lines correspond to impurity peaks of β-NaFeO2, its magnetic phase, and Na_2CO_3. The illustrations of the magnetic structures and refined parameters determined for each phase are shown in the insets.

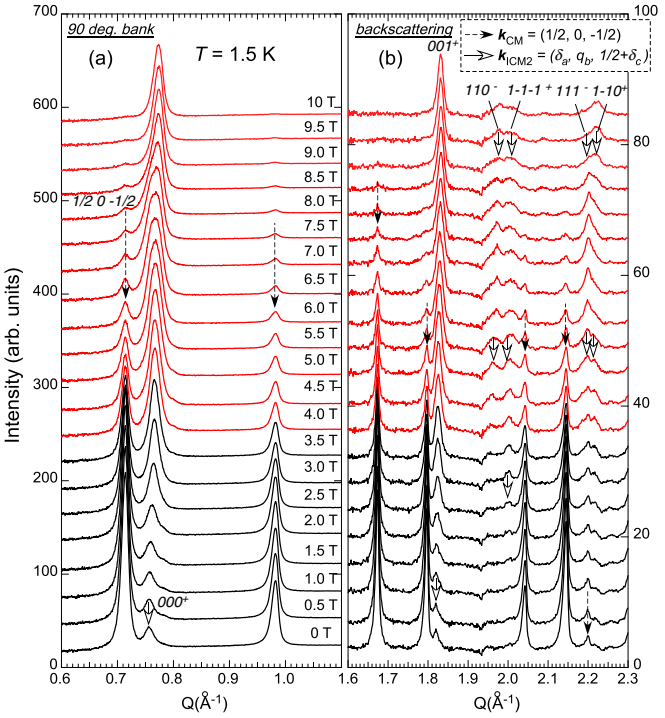

FIG. 8. (Color online) Diffraction patterns for α-$NaFeO_2$ measured in different magnetic fields using (a) 90 deg and (b) backscattering WISH detector banks, at 1.5 K. The data at 16 K in the paramagnetic phase were subtracted from the low temperature patterns. All data were measured with increasing magnetic field after cooling in zero field.

illustration of the magnetic structure are shown in Fig. 7(a). The angle between the spin direction and the a axis ϕ_{ac} was determined to be $-12^\circ \pm 6^\circ$. From the superspace symmetry description, it directly follows that the magnetic point group, controlling the macroscopic properties of the phase, is the centrosymmetric $2/m1'$, in agreement with the lack of the ferroelectric polarization above $T_{N2} = 7.5$ K [Fig. 6(c)].

The magnetic refinement for the ICM2 phase is complicated by a superposition of the magnetic peaks of this phase and either ICM1 or CM phases at any temperature in zero field and, therefore, we could not determine the magnetic structure for ICM2, conclusively. Nevertheless, the refinement was possible with the data collected in high magnetic fields, resulting in a polar cycloidal structure as discussed in the next section.

As shown in Fig. 7(b), the CM collinear magnetic ordering with the magnetic moments parallel or antiparallel to the b axis fits well the diffraction data at 1.5 K. While the spin sequence along the b axis is all-up ($\rightarrow\rightarrow\rightarrow\cdots$) or all-down ($\leftarrow\leftarrow\leftarrow\cdots$), the sequence along the a axis is two-up and two-down ($\uparrow\uparrow\downarrow\downarrow\cdots$). The stacking sequence along the c axis is antiferromagnetic. The resultant magnetic unit cell is related to the monoclinic nuclear cell as $\boldsymbol{a}_{\rm mag} = -2\boldsymbol{a}$, $\boldsymbol{b}_{\rm mag} = \boldsymbol{b}$, and $\boldsymbol{c}_{\rm mag} = -\boldsymbol{a} - 3\boldsymbol{c}$.

Figure 8 shows the magnetic field dependence of the magnetic diffraction profiles at 1.5 K. The ICM2 satellites, such as 000^+, are significantly enhanced by the magnetic field, while the intensity of the CM reflection at the $(-\frac{1}{2},0,\frac{1}{2})$ reciprocal point is reduced above 3 T, corresponding to the crossover observed in the magnetization measurements [Fig. 2(b)]. It should be noted that the ratio between the CM and ICM2 phases is slightly sample dependent and is different for the sample1 and sample2 in zero field [Fig. 9(a)]. The field dependencies of the integrated intensity of the 000^+ magnetic satellite [Fig. 9(a)] and the polarization [Fig. 9(c)] are practically identical indicating that the latter is associated with the magnetic order parameter of the ICM2 phase.

Several reflections for the ICM2 phase split under high fields; for instance, the 110^- and $1\bar{1}\bar{1}^+$ satellites are separated into two peaks above 3 T, which is shown in Fig. 8(b). This set of the reflections can be assigned to the propagation vector with three incommensurate components, $\boldsymbol{k}_{\rm ICM2} = (\delta_a, q_b, \frac{1}{2} + \delta_c)$, which are (0.0250,0.240,0.485) at $H = 5$ T. The positions of the satellite reflections of the ICM2 phase in the reciprocal space are illustrated in Fig. 5(c). We also observed a significant field dependence of the wave number q_b as shown in Fig. 9(b). With increasing magnetic field from zero up to 3 T, q_b monotonically changes from 0.231 to 0.238 and locked into 0.24 for $4.5 \leqslant H \leqslant 7.5$ T. With further increasing field, q_b

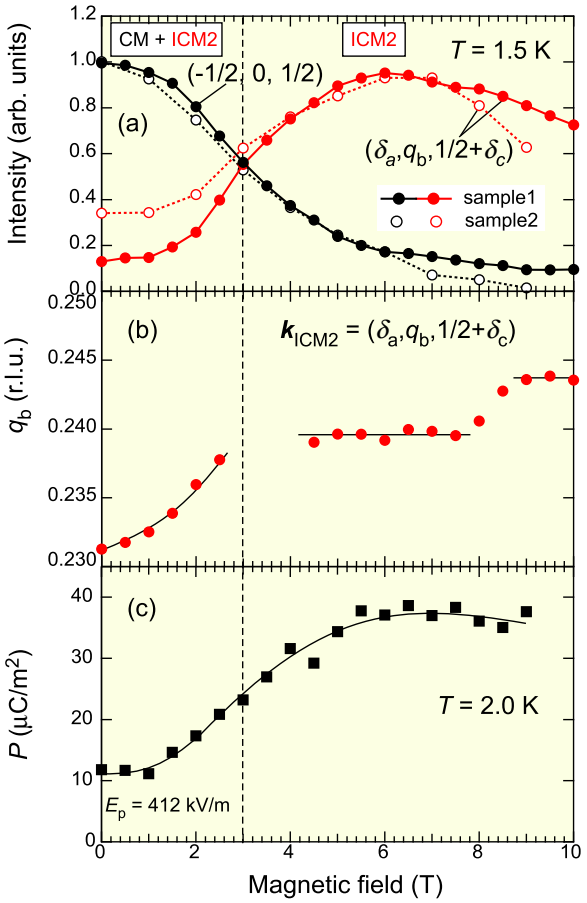

FIG. 9. (Color online) Magnetic field dependence of (a) the integrated intensity of the magnetic reflections indexed by the commensurate $\boldsymbol{k}_{\rm CM} = (-\frac{1}{2},0,\frac{1}{2})$ and the incommensurate $\boldsymbol{k}_{\rm ICM2} = (\delta_a,q_b,\frac{1}{2}+\delta_c)$ propagation vectors and (b) the wave number q_b at 1.5 K. (c) Magnetic field variation of the ferroelectric polarization at 2.0 K.

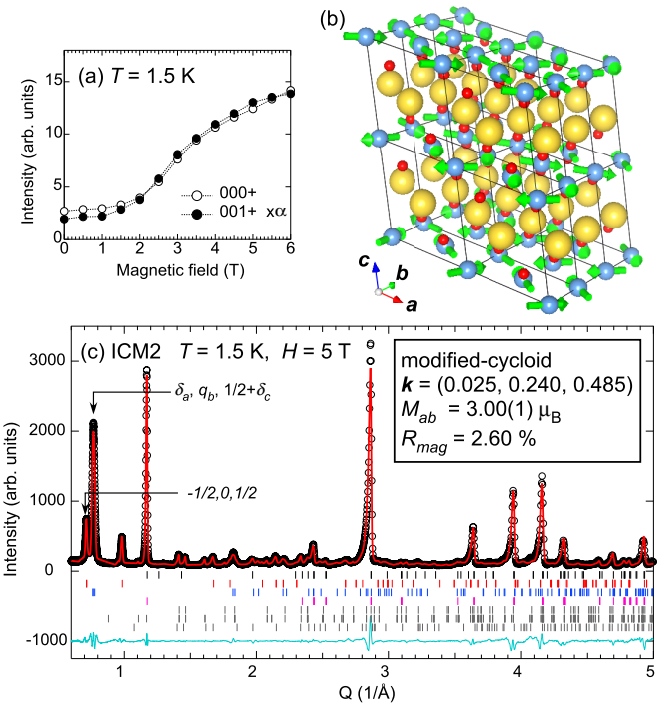

FIG. 10. (Color online) (a) Magnetic field dependence of the satellite reflections $000+\boldsymbol{k}_{\rm ICM2}$ and $001+\boldsymbol{k}_{\rm ICM2}$ [$\boldsymbol{k}_{\rm ICM2} = (\delta_a,q_b,\frac{1}{2}+\delta_c)$] at 1.5 K. The intensity of the former reflection is multiplied by a constant for appropriate scaling. (b) The modified cycloid magnetic structure as the most probable model for the ICM2 phase. The magnetic moments are rotating in the ab plane. (c) The magnetic structural refinement of the experimental data collected at $T = 1.5$ K and $H = 5$ T. The first line of the vertical bars indicates the peak positions of the main structural phase of α-$NaFeO_2$. The second, third, and fourth bar lines correspond to the CM collinear state, ab cycloid, and ferromagnetic components, respectively. The other bar lines indicate the impurity peak positions, which are explained in Fig. 7. The refined parameters and reliability factors are given in the inset.

increases again, and adopts the constant value of 0.244 above 9 T. As mentioned above, the magnetization process shows an anomaly at $H = 8$ T, which might be associated with the change in the wave number. It should be mentioned that above 7 T, two additional magnetic reflections were observed at $Q = 0.55$ and 0.75 Å^{-1} positions (not shown) whose nature is unclear at the present.

This spin arrangement is associated with the single six-dimensional irreducible representation mC_1 [order parameter direction $P2(a,-a,0,0,0,0)$] of the $R\bar{3}m1'$ space group and is identical to that reported in the previous works [26,28]. The crystal lattice keeps the monoclinic distortions detectable in the high-resolution diffraction patterns and the obtained magnetic structure possesses the following symmetry elements, twofold screw axis (2_1) along the b axis, mirror (m) perpendicular to the b axis, and inversion ($\bar{1}$), which implies the centrosymmetric magnetic space group P_a2_1/m (in the BNS notation) with the identical to the ICM1 phase point group $2/m1'$.

2. *Magnetic orderings under high magnetic field*

In general, to refine powder diffraction data for anisotropic spin systems measured under magnetic field, preferred orientation effects on relative magnetic intensities may need to be included [36]. Nevertheless, if the magnetic field does not affect the relative intensities of the magnetic peaks, as in the present case [the field variations of the 000^+ and 001^+ magnetic satellites are identical at least below 6 T, Fig. 10(a)], the field induced phase can be treated as homogeneous at a first approximation. As shown in Figs. 10(b) and 10(c), we have successfully refined the diffraction pattern measured in $H = 5$ T, using a nearly cycloidal structure with the spin components being in the (ab) plane. The "nearly" cycloid means here that the small but nonzero components δ_a and δ_c of the $\boldsymbol{k}_{\rm ICM2}$, implying an admixture of the helical components along a and c as well as the b direction. This results indicates, that in the case of α-$NaFeO_2$, the response of the system on magnetic field is not very anisotropic and the field induces the ICM2 phase in majority grains of the studied samples. This is probably because of the incommensurate structure is more "polarizable" (has a higher susceptibility) for most of the field directions in comparison with the commensurate phase. The refined value of the magnetic moments in the structure with the circular envelope is $M_{ab} = 3.00 \pm 0.01\mu_B$. The model

provides an excellent refinement quality ($R_{\text{Bragg}} = 2.60\%$) and inclusion of ellipsoidal modulation does not improve the fitting. We also tested some other models in the refinement procedure such as proper screw and cycloid structures with the spin components along the b axis and perpendicular to (ab) plane; however, all these models provide essentially worse agreement with the experimental data.

In the most symmetric case, when $\boldsymbol{k}_{\text{ICM2}}$ is on the line of symmetry [$\boldsymbol{k}_{\text{ICM2}} = (0,q_b,\frac{1}{2})$ in the monoclinic or $(q,q,\frac{3}{2})$ in the hexagonal setting], like in the case of zero field, the magnetic structure mentioned above is a proper cycloid which breaks the inversion and preserves the mirror plane (point group is $m1'$). This structure combines two irreducible order parameters $mY_1 \oplus mY_2$ of the parent $R\bar{3}m1'$ space group, implying the polar (3+1) superspace symmetry $Cm1'(0,\beta,\frac{1}{2})0s$ ($\beta = q_b$). Application of the magnetic field in a general direction breaks the mirror plane as well, resulting in the triclinic $P1(\alpha,\beta,\gamma)0$ superspace group that allows all three components of the propagation vector to be nonzero. Thus, the two additional field-induced components, δ_a and δ_c of the $\boldsymbol{k}_{\text{ICM2}}$, are the direct consequence of the symmetry of the system in the magnetic field. For more detailed discussion of this effect and its relation to the polycrystalline nature of the sample, see Ref. [37].

The temperature dependence of the magnetic diffraction patterns at 9 T is shown in Fig. 11. As clearly seen from the backscattering data, the magnetic reflections 110^- and $1\bar{1}0^+$ split into two peaks below 5.5 K, indicating the phase

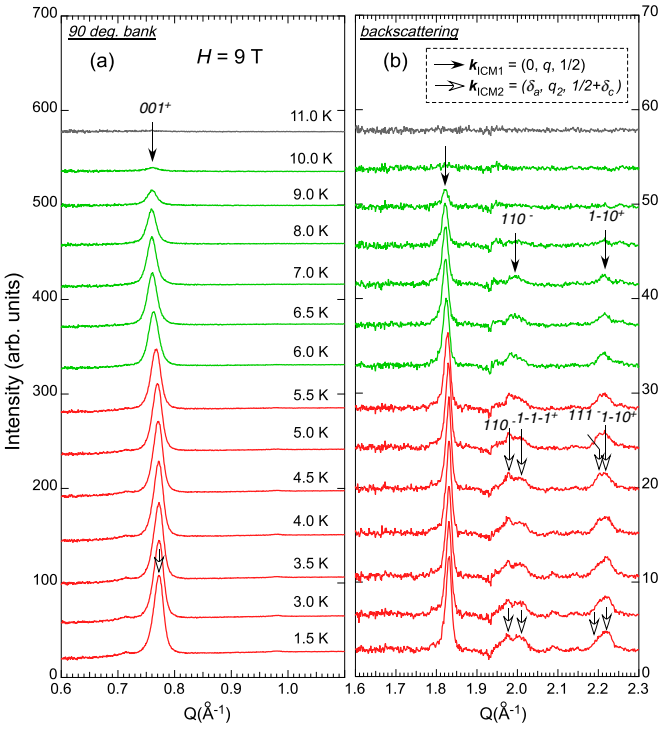

FIG. 11. (Color online) Temperature dependence of the neutron powder diffraction profiles at 9 T in α-$NaFeO_2$. The data were measured using (a) 90 deg and (b) backscattering detector banks on WISH. The data at 16 K in the paramagnetic phase were subtracted from each low temperature pattern. All data were taken on a heating process after cooling down to 1.5 K in $H = 9$ T.

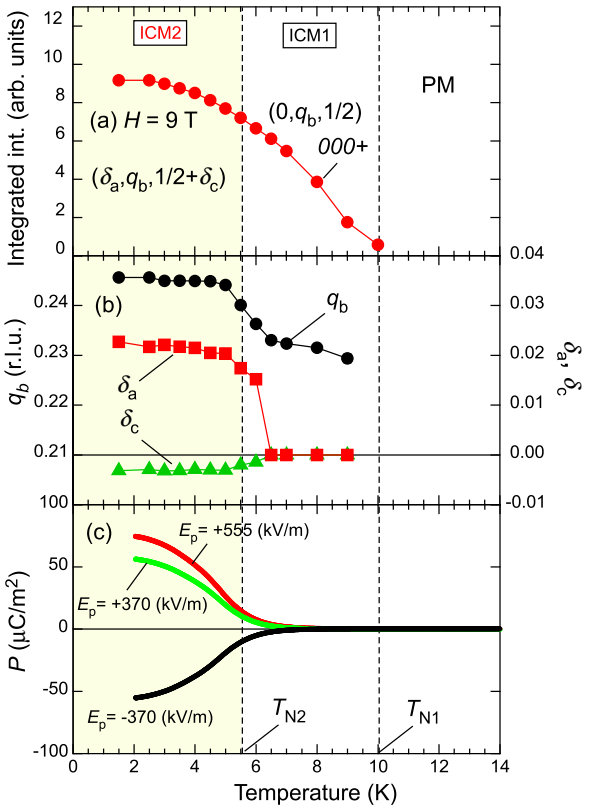

FIG. 12. (Color online) Temperature dependence of (a) the integrated intensity of the magnetic reflection 000^+, (b) the wave number q_b, and the incommensurabilities δ_a and δ_b, and (c) the electric polarization in $H = 9$ T for α-$NaFeO_2$.

transition from the ICM1 to the ICM2 phase. The wave number q_b also changes around this temperature and the parameters δ_a and δ_c start deviating from the commensurate values. These results are consistent with the appearance of the ferroelectric polarization below T_{N2}, as demonstrated in Fig. 12(c).

IV. DISCUSSION

A. Phase diagram

Based on the magnetization, dielectric, and neutron diffraction data, a ($H - T$) phase diagram has been constructed (Fig. 13). The diagram includes three magnetic phases ICM1 (spin density wave), ICM2 (cycloid), and CM (collinear antiferromagnet) with distinct stability regions. ICM1 is the high temperature phase and is the first ordered state of the system in all measured fields. In low magnetic fields $H < 2.5$ T and the intermediate temperature range $5.5 \leqslant T \leqslant 7.5$ K, ICM1 coexists with the polar ICM2 phase. The ground state of the system in zero field is CM, though this phase always coexists with ICM2, indicating an almost degenerate nature of these phases. The phase coexistence might be caused by inevitable chemical inhomogeneity in powder samples. In fact, the volume fractions of both phases slightly depends on sample, as shown in Fig. 9. For further understanding this phenomenon, systematic investigations of impurity effect on the magnetic ordering are necessary. In the case of another triangular lattice antiferromagnet $CuFeO_2$, nonmagnetic impurities drastically

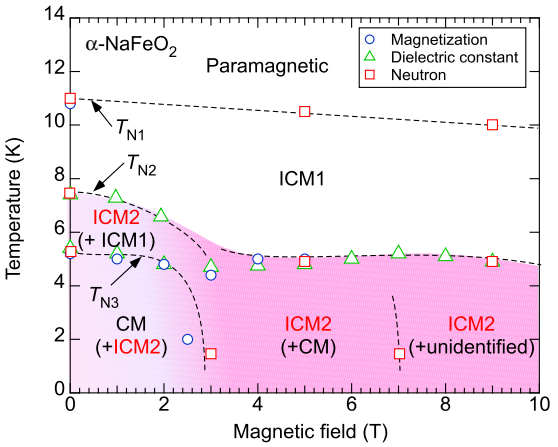

FIG. 13. (Color online) Magnetic phase diagram of polycrystalline sample of α-$NaFeO_2$. Circle, triangle, and square symbols denote the temperatures and fields where the magnetization, dielectric constant, and neutron diffraction data show anomaly, respectively. The phase boundaries are drawn by dotted lines. In the regions where the phase coexistences were observed, the minor phase is given in parentheses. The hatched area represents nonzero polarization, whose value is roughly proportional to the color contrast.

affect the magnetic ordering and causes the coexistence of the collinear ground state and the impurity induced helical state [38].

When the magnetic field is applied at low temperature, the ICM2 phase becomes the ground state of the system above 3 T, resulting in the enhancement of the ferroelectric polarization. With further increasing field, an additional magnetic phase appears above 7 T, whose nature has not been clarified in the present study due to limited information available in the powder diffraction data. To investigate this phase in more detail, higher magnetic fields or single crystal diffraction experiments are needed.

B. Mechanism of the ferroelectricity

Let us discuss the polarization behavior in α-$NaFeO_2$ based on the symmetry of the deduced magnetic structures. The centrosymmetric rhombohedral space group $R\bar{3}m1'$ of the paramagnetic phase is reduced down to the monoclinic (3+1) superspace group $C2/m1'(0,\beta,\frac{1}{2})s0s$ by the irreducible order parameter mY_1 representing the spin density wave in the ICM1 phase. The corresponding magnetic point group controlling the macroscopic properties in the system is centrosymmetric $2/m1'$ in agreement with the absence of polarization in this phase.

The neutron diffraction data in magnetic field revealed that the polar behavior is associated with the cycloidal spin arrangement in the ICM2 phase which coexists with ICM1 and CM in zero field and is the ground state of the system in high magnetic fields (Fig. 13). The (3+1) superspace group of this phase is $Cm1'(0,\beta,\frac{1}{2})0s$ which is a result of the symmetry breaking by the reducible order parameter $mY_1 \oplus mY_2$. The polar magnetic point group $m1'$ restricts the direction of the polarization to be parallel to the mirror plane ($\boldsymbol{P} \perp b$). A schematic representation of the zero

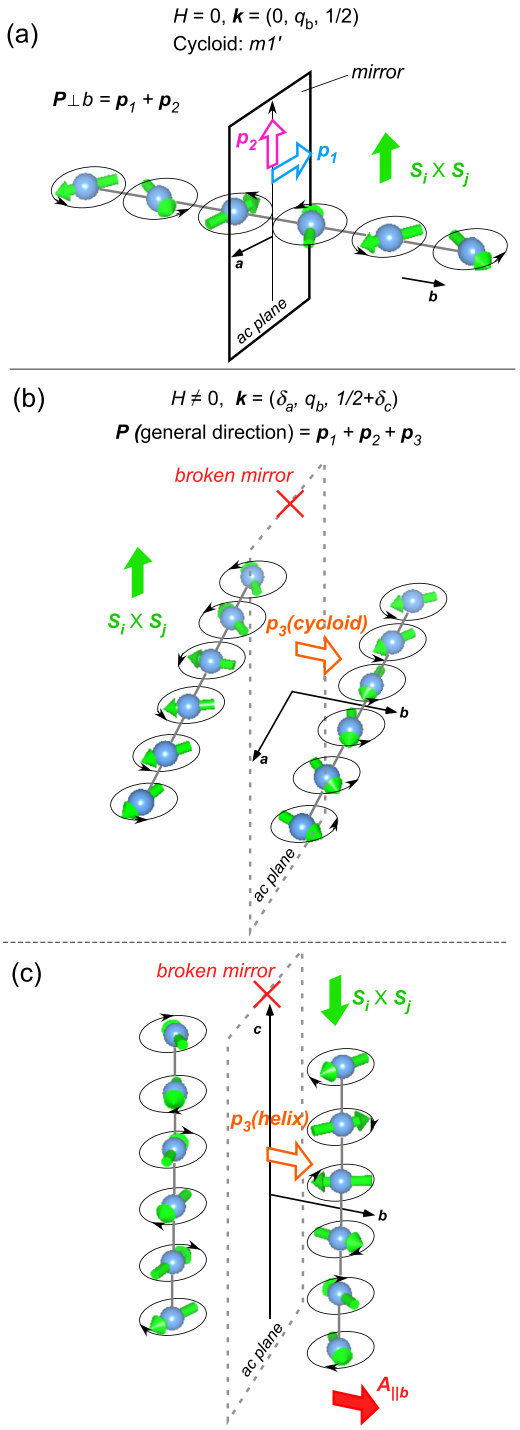

FIG. 14. (Color online) (a) Schematic illustration of the cycloidal structure of the ICM2 phase in zero magnetic field for α-$NaFeO_2$ and directions of the two electric dipole components in the ac plane, $\boldsymbol{p}_1 \propto \boldsymbol{r}_{ij} \times (\boldsymbol{S}_i \times \boldsymbol{S}_j)$ and $\boldsymbol{p}_2 \propto \boldsymbol{S}_i \times \boldsymbol{S}_j$ allowed by the magnetic symmetry. In a magnetic field, additional (b) cycloid and (c) proper screw modulations along a and c axis are induced, which generate the electric polarizations, $\boldsymbol{p}_{3(\text{cycloid})} \propto \boldsymbol{r}_{ij} \times (\boldsymbol{S}_i \times \boldsymbol{S}_j)$ and $\boldsymbol{p}_{3(\text{helix})} \propto [\boldsymbol{r}_{ij} \cdot (\boldsymbol{S}_i \times \boldsymbol{S}_j)]\boldsymbol{A}$, respectively.

field cycloid structure in the ICM2 phase is illustrated in Fig. 14(a). The spin current mechanism [6] and the theory of inverse DM effect [5] developed for the orthorhombic $Pbmn$ perovskites both predict $\boldsymbol{p} \propto \boldsymbol{r}_{ij} \times (\boldsymbol{S}_i \times \boldsymbol{S}_j) (\equiv \boldsymbol{p}_1)$, i.e., $\boldsymbol{P}$ to be

perpendicular to both $\boldsymbol{r}_{ij}$ and $\boldsymbol{S}_i \times \boldsymbol{S}_j$, and therefore confined along the $-a$ direction in Fig. 14. Nonetheless, the deduced point symmetry does not restrict $\boldsymbol{P}$ to the $-a$ direction only and allows the orthogonal component, parallel to $\boldsymbol{S}_i \times \boldsymbol{S}_j$. Thus, based on the symmetry argument, one can introduce additional contribution to the macroscopic polarization $\boldsymbol{p}_2 \propto \boldsymbol{S}_i \times \boldsymbol{S}_j$. Kaplan and Mahanti [19] have shown that this additional term $\boldsymbol{p}_2$ contributes to macroscopic polarization in both cycloid and proper screw helical cases, unless mirror plane containing $\boldsymbol{r}_{ij}$ or twofold rotation axis perpendicular to $\boldsymbol{r}_{ij}$ exists. Therefore, the direction of the polarization in α-$NaFeO_2$ is not expected to follow the well known expression [4–6]. Although the mechanism regarding the appearance of $\boldsymbol{P}$ is the inverse DM effect, its direction is determined by the sum of the two orthogonal components $\boldsymbol{p}_1 + \boldsymbol{p}_2$. It should be pointed out here that the $\boldsymbol{p}_2$ component parallel to $\boldsymbol{S}_i \times \boldsymbol{S}_j$ is also applicable to other delafossite compounds ABO_2 (A = Cu, Ag, B = Fe, Cr) where the spin ordering breaks the threefold and inversion symmetry [11–14,16,17,22].

Application of the magnetic field at low temperature stabilizes the ICM2 phase and reduces its symmetry down to the triclinic $P1(\alpha,\beta,\gamma)0$. The latter allows $\delta_a = \alpha$ and $\delta_c = \gamma - \frac{1}{2}$ to be nonzero resulting in admixture of the another cycloidal and the proper screw components. They generate an additional contribution $\boldsymbol{p}_3$ to the macroscopic polarization, perpendicular to both $\boldsymbol{p}_1$ and $\boldsymbol{p}_2$ through the classical inverse DM effect [4–6] $\boldsymbol{p}_{3(\text{cycloid})} \propto \boldsymbol{r}_{ij} \times (\boldsymbol{S}_i \times \boldsymbol{S}_j)$ generated by the cycloidal modulation propagating along the a axis, and the ferroaxial mechanism [9,10] $\boldsymbol{p}_{3(\text{helix})} \propto [\boldsymbol{r}_{ij} \cdot (\boldsymbol{S}_i \times \boldsymbol{S}_j)]\boldsymbol{A}$ induced by the proper screw component propagating along the c axis. [Figs. 14(b) and 14(c)]. Therefore, the polarization in the field induced ICM2 phase is not restricted and takes a general direction, namely $\boldsymbol{p}_{\text{total}} = \boldsymbol{p}_1 + \boldsymbol{p}_2 + \boldsymbol{p}_{3(\text{cycloid})} + \boldsymbol{p}_{3(\text{helix})}$. The additional polarization $\boldsymbol{p}_3$ induced by the magnetic field applied in a general direction phenomenologically is described by the free-energy coupling invariants $b_{212}H_bH_aP_b + b_{232}H_bH_cP_b$ (where $H_{a,b,c}$ are components of the magnetic field, b_{212}, b_{232} are phenomenological coefficients, and $\boldsymbol{P}_b \equiv \boldsymbol{p}_3$) allowed by the $m1'$ point group. Thus, the field-induced symmetry lowering of the incommensurate propagation vector resulting in admixture of the cycloidal and proper screw components of the magnetic order parameter represents the mechanism of this bilinear magnetoelectric effect. The thermodynamical aspects of this phenomena is discussed in Ref. [37]. The linear-quadratic magnitoelectric coupling invariants of the $H_bH_{a(c)}P_b$ form indicate that $\boldsymbol{p}_3$ can be switched by flipping one of the field components (H_b or $H_{a,c}$), which implies changing of the spin chirality of the field-induced cycloidal and proper screw components.

C. Stability of the magnetic ground state

The CM collinear antiferromagnetic structure in α-$NaFeO_2$ is essentially different from the ground state of the closely related delafosite compound $CuFeO_2$. The difference relates to both the propagation vector $\boldsymbol{k} = (-\frac{1}{2},0,\frac{1}{2})$ in α-$NaFeO_2$ and $\boldsymbol{k} = (0,\frac{1}{2},\frac{1}{2})$ in $CuFeO_2$, and the respective spin directions along the hexagonal [110] (monoclinic b) and [001] (monoclinic c) axes. The main reason for the difference is apparently the sign of the nearest neighbor exchange parameter J_1, which is negative in $CuFeO_2$ [39,40] and positive in α-$NaFeO_2$ according to the mean field calculation by Tomkowicz and Vanlaar [26].

As it has been discussed by Mekata *et al.* [23], the nearest neighbor exchange interaction in the basal plane of $CuFeO_2$ is a sum of ferromagnetic direct exchange and antiferromagnetic 90° superexchange. Although the 180° superexchange interaction between octahedrally coordinated Fe^{3+} spins is well known to be strongly antiferromagnetic [41], the 90° superexchange between $3d^5$ spins involves several competitive mechanisms and its sign is difficult to predict [41,42]. The interatomic distances between the nearest neighbor Fe ions determined from the refinement of the high resolution neutron diffraction data are 3.01824(33) in α-$NaFeO_2$ and 3.02980(4) in $CuFeO_2$, at 16 K. The ferromagnetic direct exchange in α-$NaFeO_2$, therefore, is expected to be stronger than in $CuFeO_2$. The bond angles Fe^{3+}-O^{2-}-Fe^{3+} in α-$NaFeO_2$ and $CuFeO_2$ are $\simeq$96.8° and $\simeq$93.2°, respectively. The difference in the bond angles favors a weaker antiferromagnetic superexchange interaction in α-$NaFeO_2$. Thus, the sum of the stronger ferromagnetic direct exchange and the weaker antiferromagnetic superexchange in α-$NaFeO_2$ might result in the change of the sign for the nearest neighbor exchange parameter.

In respect of the experimentally found direction of the spins in the ground state of α-$NaFeO_2$, we found a placeable explanation based on anisotropic dipole-dipole interaction. Indeed, since a strong magnetocrystalline anisotropy through spin-orbit coupling is not expected in the system of the orbitally singlet Fe^{3+} ions, the magnetic dipole interaction can provide the predominant contribution to the magnetic anisotropy taking into account the relatively large magnetic moment of these ions. To verify this assumption, we numerically calculated the magnetic dipole energy of the CM ground state of α-$NaFeO_2$, using the following expression:

$$E_D = \frac{1}{2}(g\mu_B)^2 \sum_{i \neq j}^{n} \frac{1}{r_{ij}^3}\left(\boldsymbol{S}_i \cdot \boldsymbol{S}_j - \frac{3(\boldsymbol{S}_i \cdot \boldsymbol{r}_{ij})(\boldsymbol{S}_j \cdot \boldsymbol{r}_{ij})}{r_{ij}^2}\right).$$

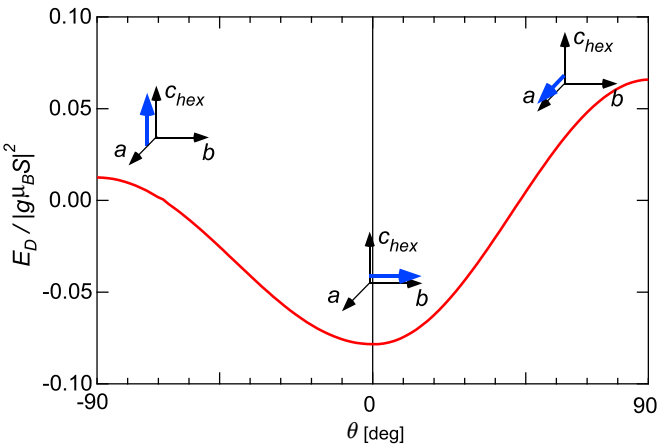

FIG. 15. (Color online) The spin direction dependence of the magnetic dipole energy. For $-90° \leqslant \theta \leqslant 0°$, θ corresponds to the angle tilted toward the hexagonal c axis from the b axis, and the angle toward the a axis for $0° \leqslant \theta \leqslant 90°$. The calculation was carried out with the system size of 1352 sites.

Evaluation of E_D for different sizes of the system up to 10^4 spins confirmed that E_D becomes practically constant above the 10^3 number of spins. Figure 15 demonstrates the dependence of E_D on the tilting angle θ of the spins from the monoclinic b axis. One can clearly see that the energy minimum corresponds to $\theta = 0$ in agreement with the experimentally found spin direction.

V. CONCLUSION

Geometrically frustrated antiferromagnet α-$NaFeO_2$ exhibits a sequence of magnetostructural phase transitions induced by temperature and magnetic field. The highest temperature transition occurring at $T_{N1} = 11$ K results in a long range incommensurate magnetic ordering (ICM1) with collinear sine modulated moments, reducing the paramagnetic rhombohedral $R\bar{3}m1'$ symmetry down to the nonpolar (3+1) magnetic superspace group $C2/m1'(0,\beta,\frac{1}{2})s0s$. Below $T_{N2} = 7.5$ K, ICM1 phase coexists with the polar $Cm1'(0,\beta,\frac{1}{2})0s$ cycloidal ordering (ICM2). It turns into collinear commensurate (CM) ground state with the nonpolar P_a2_1/m symmetry at $T_{N3} = 5.5$ K. A small amount of ICM2 always coexists with the ICM1 and CM phase producing a nonzero polarization below T_{N2} in zero magnetic field. The difference between the collinear ground state in α-$NaFeO_2$ and the closely related delafossite $CuFeO_2$ is attributed to different signs of the nearest neighbor interactions and the predominant contribution of the dipolar interactions to the magnetic anisotropy in the case of α-$NaFeO_2$. Magnetic field destabilizes the collinear ground state and promotes the polar ICM cycloidal phase resulting in a drastic increase of the polarization. The symmetry of the zero field cycloidal spin structure allows the two orthogonal components $\boldsymbol{p}_1 \propto \boldsymbol{r}_{ij}\times(\boldsymbol{S}_i\times\boldsymbol{S}_j)$ and $\boldsymbol{p}_2 \propto \boldsymbol{S}_i\times\boldsymbol{S}_j$ to contribute to the macroscopic polarization through the inverse DM effect. The applied magnetic field reduces the symmetry of the ICM2 phase down to the triclinic $P1(\alpha,\beta,\gamma)0$, resulting in admixture of additional cycloidal and proper screw components both generating magnetic field switchable polarization $\boldsymbol{p}_3$ perpendicular to $\boldsymbol{p}_1$ and $\boldsymbol{p}_2$.

ACKNOWLEDGMENTS

The images shown in Figs. 1, 7, 10, and 14 were depicted using the software VESTA [43] developed by K. Monma. This work was supported by an international collaboration research program, "Young Researcher Overseas Visits Program for Vitalizing Brain Circulation" of JSPS. N.T. was supported by the JSPS Postdoctoral Fellowships for Research Abroad.

[1] T. Kimura, T. Goto, H. Shintani, K. Ishizaka, T. Arima, and Y. Tokura, Nature (London) **426**, 55 (2003).
[2] S.-W. Cheong and M. Mostovoy, Nat. Mater. **6**, 13 (2007).
[3] Y. Tokura and S. Seki, Adv. Mater. **22**, 1554 (2010).
[4] M. Mostovoy, Phys. Rev. Lett. **96**, 067601 (2006).
[5] I. A. Sergienko and E. Dagotto, Phys. Rev. B **73**, 094434 (2006).
[6] H. Katsura, N. Nagaosa, and A. V. Balatsky, Phys. Rev. Lett. **95**, 057205 (2005).
[7] M. Kenzelmann, G. Lawes, A. B. Harris, G. Gasparovic, C. Broholm, A. P. Ramirez, G. A. Jorge, M. Jaime, S. Park, Q. Huang, A. Ya. Shapiro, and L. A. Demianets, Phys. Rev. Lett. **98**, 267205 (2007).
[8] A. J. Hearmon, F. Fabrizi, L. C. Chapon, R. D. Johnson, D. Prabhakaran, S. V. Streltsov, P. J. Brown, and P. G. Radaelli, Phys. Rev. Lett. **108**, 237201 (2012).
[9] R. D. Johnson, S. Nair, L. C. Chapon, A. Bombardi, C. Vecchini, D. Prabhakaran, A. T. Boothroyd, and P. G. Radaelli, Phys. Rev. Lett. **107**, 137205 (2011).
[10] R. D. Johnson, L. C. Chapon, D. D. Khalyavin, P. Manuel, P. G. Radaelli, and C. Martin, Phys. Rev. Lett. **108**, 067201 (2012).
[11] T. Kimura, J. C. Lashley, and A. P. Ramirez, Phys. Rev. B **73**, 220401(R) (2006).
[12] S. Kanetsuki, S. Mitsuda, T. Nakajima, D. Anazawa, H. A. Katori, and K. Prokes, J. Phys.: Condens. Matter **19**, 145244 (2007).
[13] S. Seki, Y. Yamasaki, Y. Shiomi, S. Iguchi, Y. Onose, and Y. Tokura, Phys. Rev. B **75**, 100403(R) (2007).
[14] N. Terada, T. Nakajima, S. Mitsuda, H. Kitazawa, K. Kaneko, and N. Metoki, Phys. Rev. B **78**, 014101 (2008).
[15] T. Nakajima, S. Mitsuda, K. Takahashi, M. Yamano, K. Masuda, H. Yamazaki, K. Prokes, K. Kiefer, S. Gerischer, N. Terada, H. Kitazawa, M. Matauda, K. Kakurai, H. Kimura, Y. Noda, M. Soda, M. Matsuura, and K. Hirota, Phys. Rev. B **79**, 214423 (2009).
[16] S. Seki, Y. Onose, and Y. Tokura, Phys. Rev. Lett. **101**, 067204 (2008).
[17] K. Kimura, H. Nakamura, K. Ohgushi, and T. Kimura, Phys. Rev. B **78**, 140401(R) (2008).
[18] T. Arima, J. Phys. Soc. Jpn. **76**, 073702 (2007).
[19] T. A. Kaplan and S. D. Mahanti, Phys. Rev. B **83**, 174432 (2011).
[20] M. F. Collins and O. A. Petrenko, Can. J. Phys. **75**, 605 (1997).
[21] M. Soda, K. Kimura, T. Kimura, M. Matsuura, and K. Hirota, J. Phys. Soc. Jpn. **78**, 124703 (2009).
[22] N. Terada, D. D. Khalyavin, P. Manuel, Y. Tsujimoto, K. Knight, P. G. Radaelli, H. S. Suzuki, and H. Kitazawa, Phys. Rev. Lett. **109**, 097203 (2012).
[23] M. Mekata, N. Yaguchi, T. Takagi, T. Sugino, S. Mitsuda, H. Yoshizawa, N. Hosoito, and T. Shinjo, J. Phys. Soc. Jpn. **62**, 4474 (1993).
[24] F. Ye, Y. Ren, Q. Huang, J. A. Fernandez-Baca, P. Dai, J. W. Lynn, and T. Kimura, Phys. Rev. B **73**, 220404(R) (2006).
[25] M. Poienar, F. Damay, C. Martin, V. Hardy, A. Maignan, and G. Andre, Phys. Rev. B **79**, 014412 (2009).
[26] Z. Tomkowicz and B. Vanlaar, Phys. Status Solidi A **23**, 683 (1974).
[27] T. Ichida, T. Shinjo, Y. Bando, and T. Takada, J. Phys. Soc. Jpn. **29**, 795 (1970).
[28] T. McQueen, Q. Huang, J. W. Lynn, R. F. Berger, T. Klimczuk, B. G. Ueland, P. Schiffer, and R. J. Cava, Phys. Rev. B **76**, 024420 (2007).
[29] Y. Takeda, J. Akagi, A. Edagawa, M. Inagaki, and S. Naka, Mat. Res. Bull. **15**, 1167 (1980).
[30] R. M. Ibberson, W. I. F. David, and K. S. Knight, *The High-Resolution Powder Diffractometer (HRPD) at ISIS User Guide, Report, RAL-92-031* (Rutherford Appleton Laboratory, Chilton, Didcot, England, 1992).

[31] L. C. Chapon, P. Manuel, P. G. Radaelli, C. Benson, L. Perrott, S. Ansell, N. J. Rhodes, D. Raspino, D. Duxbury, E. Spill, and J. Norris, Neutron News **22**, 22 (2011).
[32] O. Kirichek, J. Brown, D. T. Adroja, P. Manuel, G. Kouzmenko, R. I. Bewley, and R. Wotherspoon, J. Phys.: Conf. Ser. **400**, 052013 (2012).
[33] J. Rodriguez-Carvajal, Physica B **192**, 55 (1993).
[34] B. J. Campbell, H. T. Stokes, D. E. Tanner, and D. M. Hatch, J. Appl. Crystallogr. **39**, 607 (2006).
[35] J. M. Perez-Mato, J. L. Ribeiro, V. Petricek, and M. I. Aroyo, J. Phys.: Condens. Matter **24**, 163201 (2012).
[36] M. Lenertz, J. Alaria, D. Stoeffler, S. Colis, A. Dinia, O. Mentre, G. Andre, F. Porcher, and E. Suard, Phys. Rev. B **86**, 214428 (2012).
[37] D. D. Khalyavin *et al.* (unpublished).
[38] T. Nakajima, S. Mitsuda, K. Takahashi, K. Yoshitomo, K. Masuda, C. Kaneko, Y. Honma, S. Kobayashi, H. Kitazawa, M. Kosaka, N. Aso, Y. Uwatoko, N. Terada, S. Wakimoto, M. Takeda, and K. Kakurai, J. Phys. Soc. Jpn. **81**, 094710 (2012).
[39] F. Ye, J. A. Fernandez-Baca, R. S. Fishman, Y. Ren, H. J. Kang, Y. Qiu, and T. Kimura, Phys. Rev. Lett. **99**, 157201 (2007).
[40] T. Nakajima, A. Suno, S. Mitsuda, N. Terada, S. Kimura, K. Kaneko, and H. Yamauchi, Phys. Rev. B **84**, 184401 (2011).
[41] J. Kanamori, J. Phys. Chem. Solids **10**, 87 (1959).
[42] J. B. Goodenough, *Magnetism and the Chemical Bond* (Interscience, New York, 1963).
[43] K. Momma and F. Izumi, J. Appl. Crystallogr. **41**, 653 (2008).